How to make a dial not a switch: Control of histidine kinase conformation by an ABC-transporter facilitates need-based activation of antibiotic resistance

Alan Koh[1,2], Marjorie J. Gibbon[1,2], Marc W. Van der Kamp[3], Christopher R. Pudney[1], Susanne Gebhard[1,2]*

[1]Department of Biology and Biochemistry, [2]Milner Centre for Evolution, University of Bath, Claverton Down, Bath, BA2 7AY, United Kingdom; [3]School of Biochemistry, University of Bristol, University Walk, Bristol, BS8 1TD, United Kingdom.

*Corresponding author. Phone: +44 1225 386421; E-mail: s.gebhard@bath.ac.uk

Running title: Kinase control by an ABC-transporter

Keywords: Signal transduction, flux-sensing, antimicrobial peptide, cell envelope stress

ABSTRACT

Bacteria exert close control over gene expression to ensure optimal physiological responses to their environment, balancing metabolic costs against physiological gain. Classically we consider such regulatory responses as being switch-like, with gene expression on or off. Is it possible for such responses to be more analog and act as graded dials rather than digital switches? If it is, how might this work? We previously described a novel regulatory logic that produces an analog response, where the signaling output is gradually dialed up over an input dynamic range of several orders of magnitude. This extraordinarily fine-tuned response is achieved via a two-component regulatory system that forms a sensory complex with an ABC-transporter, where signaling is proportional to transport activity. The resulting gradual tuning of gene expression leads to a very cost-effective activation of antibiotic resistance in response to the cell's need for detoxification capacity. Here, we show how such analog signaling behavior can be achieved mechanistically. Using experimentation and computation we show that the histidine kinase within the sensory complex is activated by piston-like displacements in the membrane, which are converted to helical rotations in the catalytic core via an intervening HAMP-like domain. Intriguingly, the transporter was found not only to be required for kinase activation, but also to actively maintain the kinase in its inactive state in the absence of the drug. Such slaving of kinase activity to that of the transporter will allow the level of complete control required to achieve transport flux-dependent analog signaling. Moreover, we show that the transporter has evolved for sub-maximal signaling sensitivity, highlighting yet another layer of fine-tuning and energy-conservation in signaling. These results provide the first mechanistic overview of the design principles of an analog dial, which has importance in energy-efficient decision making in bacteria more broadly, and antibiotic resistance and synthetic biology more specifically.

41 **INTRODUCTION**

42 Bacteria have exquisite abilities to physiologically respond to environmental conditions to
43 ensure their survival and proliferation. Decision-making has to balance the benefits of a
44 particular response against the metabolic cost of the associated changes in gene expression.
45 To achieve this, bacteria employ regulatory systems that can detect extracellular or
46 intracellular information and modulate the expression of a defined set of target genes. In the
47 simplest case, regulation is dependent on the presence or absence of a ligand, and this is often
48 thought of as a digital response, where gene expression is either switched ON or OFF.
49 However, some regulatory systems display a much more analog behavior, where the output is
50 gradually dialed up in response to the strength of the input information. While it is
51 straightforward to explain digital switch behavior, e.g. DNA-binding of a regulator in the
52 presence of a ligand, it is much harder to envision what molecular mechanisms may realize a
53 gradated, analog response.

54 We previously described a new sensory strategy that produces an unprecedented degree of
55 fine-tuning, with three orders of magnitude of output modulation over an input dynamic
56 range of three orders of magnitude [1]. This regulatory logic is achieved by a two-component
57 system whose histidine kinase works in a sensory complex with an ABC-transporter [1,2] (Fig.
58 1). Such systems are wide-spread among low G+C content Gram-positive bacteria, such as
59 bacilli, lactobacilli, staphylococci, streptococci, enterococci and clostridia [3-8]. They are
60 collectively referred to as Bce-like systems and impart resistance against a broad range of cell
61 wall-active peptide antibiotics [9,10]. Based on computational modelling of the response
62 dynamics, we have established that signaling is proportional to transport activity [1]. Because
63 the transporter mediates the actual resistance, presumably by removal of the antibiotic from
64 its target in the cell envelope [1,11-13], increased transporter production acts a negative feedback

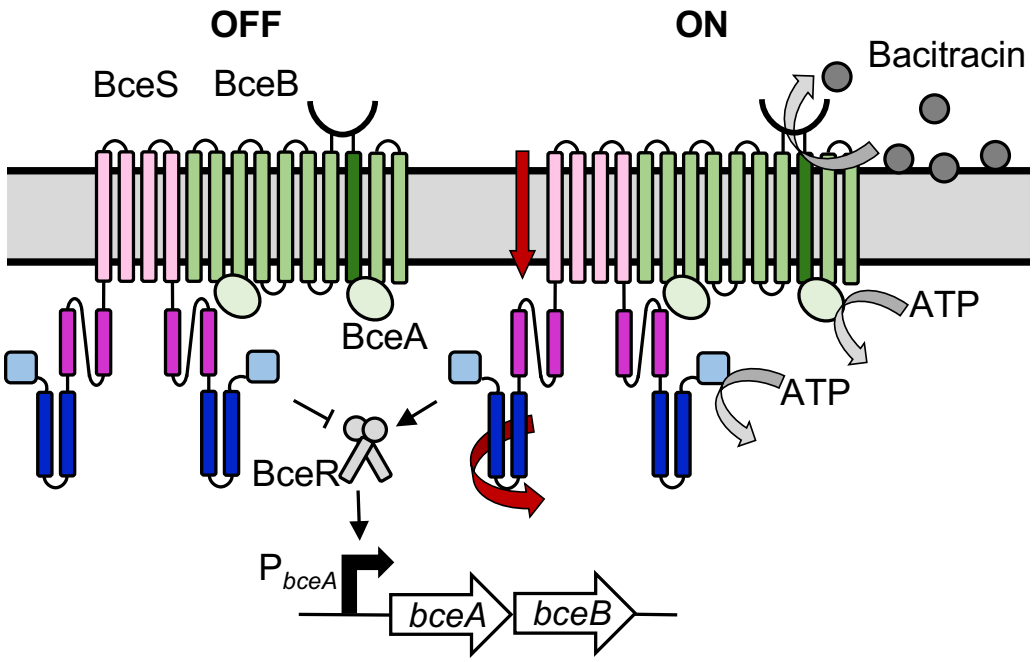

Figure 1. Function of the BceRS-BceAB resistance system of *B. subtilis.* BceS and its domains are shown in shades of pink and blue, with the HAMP-like domain in dark pink, and DHp domain in dark blue; BceAB is in green with the 8th transmembrane helix marked in dark green. The left section of the schematic shows the system in its inactive (OFF) state; the right shows the active (ON) state in the presence of antibiotics, exemplified by bacitracin. ATP hydrolysis reactions and antibiotic removal are indicated by grey arrows; for simplicity ATP hydrolysis is only shown for one ATPase each. The motions of kinase domains upon activation are shown as red block arrows.

65 on signaling, which creates the characteristic gradual, fine-tuned response [1]. This flux-
66 sensing mechanism effectively allows the bacterium to adjust its response according to its
67 need for additional detoxification capacity, implementing a cost-effective 'produce-to-
68 demand' strategy. However, the molecular mechanism of this new signaling strategy, i.e. how
69 the histidine kinase is activated within the sensory complex and how this creates the observed
70 analog response behavior, remains unknown.

71 Histidine kinases typically relay extracellular information to the cytoplasm via
72 autophosphorylation at a conserved histidine residue. The phosphoryl group is then
73 transferred to a cytoplasmic response regulator, usually a DNA-binding protein that elicits
74 changes in gene expression [14]. Despite their importance in bacterial signaling, we still have
75 limited understanding of the molecular mechanisms by which histidine kinases transmit
76 information through the cytoplasmic membrane. This is in part due to the modular
77 architecture of the kinases, which allows a plethora of different input domains to be coupled
78 to a conserved catalytic core. The core consists of a DHp (also known as HisKA) domain that
79 facilitates dimerization and histidine phosphotransfer, and a C-terminal ATPase domain [14].
80 The extracellular input and cytoplasmic core domains are separated by transmembrane
81 segments and usually at least one cytoplasmic signal transfer domain (e.g. HAMP or PAS
82 domains) [14,15]. While we still have no knowledge of the complete set of conformational
83 changes during transmembrane signaling by histidine kinases, recent studies of domains in
84 isolation or in context with an adjacent domain suggest a combination of rotating and
85 scissoring motions and piston-like helical displacements [15-18].

86 Most histidine kinases respond directly to an environmental cue via their input domains, but
87 some are controlled by accessory proteins, which are often transporters [19,20]. The majority of
88 transporters with a signaling role act as repressors of kinase activity, and deletion of the

89 transporter leads to constitutive activation of signaling [21-23]. While the molecular mechanisms
90 are unknown, it is conceivable that such transporters act as a physical block on their
91 respective kinases, and that this block is disrupted during active transport, allowing signaling
92 to proceed. In the flux-sensing Bce-like systems, however, the histidine kinases fully rely on
93 their cognate transporters for activation, and remain inactive when the transporter is deleted
94 [9,24]. Moreover, implementing the reported flux-sensing strategy requires kinase activity to be
95 directly proportional to transport activity [1]. To our knowledge, no information is available on
96 how accessory proteins may achieve such positive and precise control over a histidine kinase.

97 In the present study, we sought to understand the mechanistic basis of histidine kinase
98 activation in the Bce system of *Bacillus subtilis* and how this links to the system's analog
99 signaling behavior. Through computational predictions, detailed mutagenesis and cysteine
100 cross-linking and accessibility analyses, we provide evidence that the kinase BceS is
101 activated via helical rotations in the DHp domain, accompanied by a piston movement in the
102 second transmembrane domain. Physical motions are most likely relayed via a poorly-
103 conserved intervening HAMP-like domain. To our knowledge this is the first report of a
104 complete set of conformational changes *in vivo* during activation of a membrane-bound
105 histidine kinase. Artificial activation of the kinase through charge substitutions in the DHp
106 domain revealed that the transporter not only acts as the activator of the kinase, but also
107 controls its inactive state. We propose it is this complete control over kinase conformation
108 that slaves its activity to that of the transporter. Surprisingly, mutagenesis of the putative
109 signaling domain of the transporter, BceAB, highlighted that the system has not evolved for
110 maximal signaling sensitivity, which likely represents an additional layer of fine-tuning and
111 minimizing energy expenditure in control of antibiotic resistance.

112

113 **RESULTS**

114 **Generation and validation of a BceS homology model.** Analysis of the domain architecture
115 of BceS using SMART [25] showed two N-terminal transmembrane helices, predicted to end at
116 residue F55, and a prototypical cytoplasmic kinase core with a DHp domain from residues
117 E115 to I172 and ATPase domain from S216 to N326. The 60 amino acid linker between the
118 transmembrane and DHp domains contained no predicted domains. A recent NMR structure
119 of the homologous kinase NsaS from *Staphylococcus aureus* reported the existence of a
120 coiled-coil conformation in this region of the protein [17]. However, with 23 amino acids the
121 linker in NsaS is much shorter than that in BceS. To investigate the cytoplasmic composition
122 of BceS in more detail, we used I-TASSER [26] to predict the tertiary structure of the linker
123 region and DHp domain (residues R56 to N174; Fig. 2a). The closest structural analog was
124 the hybrid kinase Af1503-EnvZ from *Archaeoglobus fulgidus* and *E. coli*, respectively (PDB
125 3ZRW). BceS showed the typical DHp domain fold of two antiparallel helices (DHp1 and
126 DHp2), joined by a short loop. In the functional kinase dimer, this will form the four-helix
127 bundle characteristic for most histidine kinases [14] (Fig.2c). Interestingly, the linker between
128 the membrane interface and DHp domain adopted a HAMP-like conformation with two short
129 parallel helices (HAMP1 and HAMP2), where HAMP2 continues into DHp1 as a single
130 continuous helix (Fig. 2a). The relevance of this domain, which had not been predicted in
131 previous analyses, is discussed in more detail below.

132 To test the accuracy of the homology model, we probed the relative orientation of helices
133 within the DHp domain four-helix bundle, based on proximity of individual residues, using
134 oxidative cysteine crosslinking. These experiments were done *in vivo* using cells deleted for
135 the native copy of *bceS* and carrying a single-copy ectopic construct for expression of *bceS*
136 with a C-terminal His_8-tag, allowing slight over-production of the kinase to facilitate

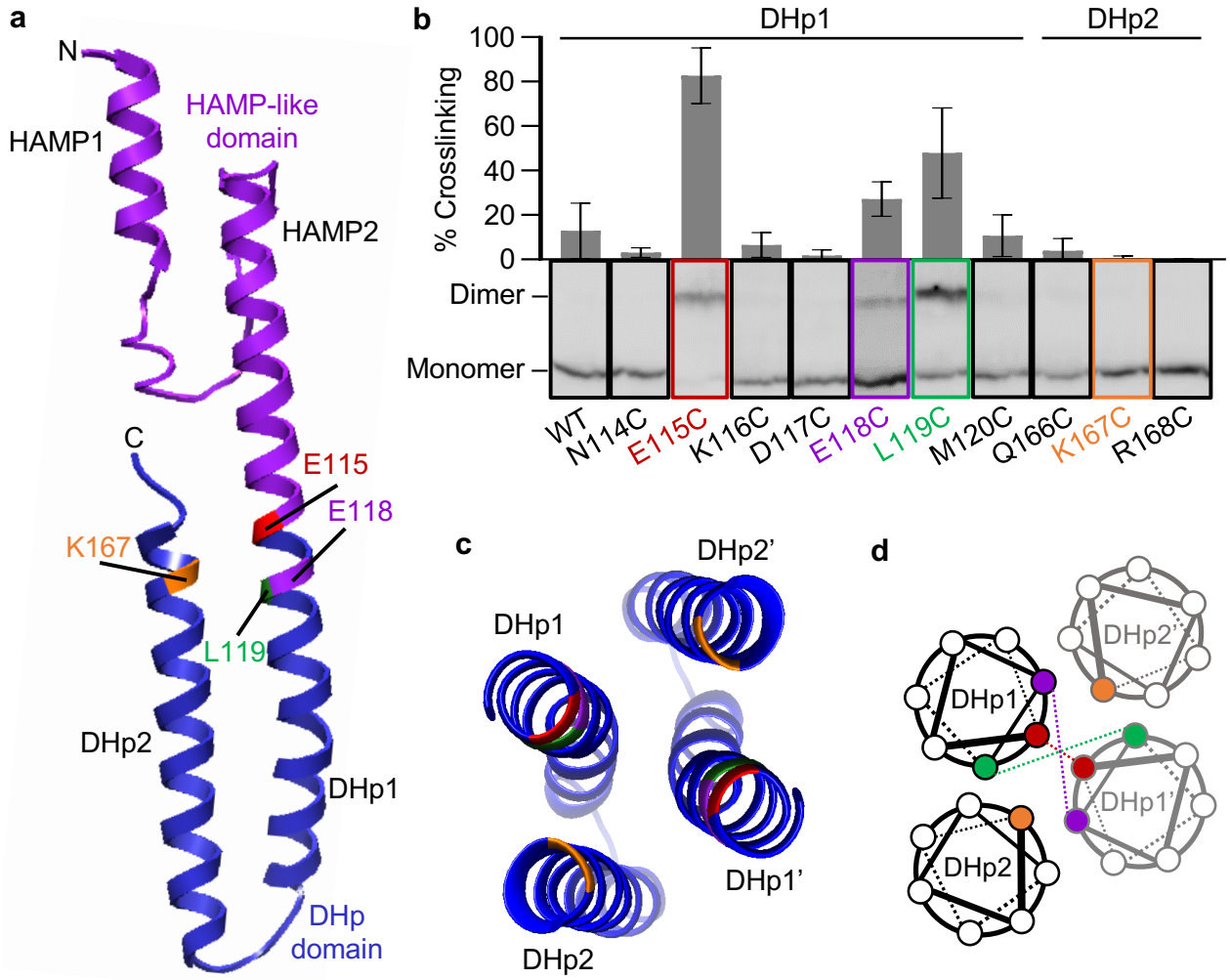

Figure 2: BceS DHp domain forms a four-helix bundle. a, Homology model of the BceS HAMP-like and DHp domains generated by I-TASSER (C-score = -0.76). The HAMP-like domain is shown in purple and the DHp domain in blue. The residues that form Cys-crosslinks in panel b are highlighted, E115 (red), E118 (purple) and L119 (green). Residue K167, which sits opposite E115, is shown in orange. **b**, Percentage of crosslinking for each BceS Cys variant was calculated from relative band intensities between monomer and dimer within each lane using Fiji [42]. Amino acid substitutions were introduced in parent construct *bceS*^{WT}-His$_8$ (SGB369) and BceS production was controlled by addition of 0.02 % (w/v) xylose. Data are shown as mean ± SD from 2-5 independent repeats. **c, d**, Schematic diagram of the BceS DHp dimer configuration. Helices labelled DHp1' and DHp2' show the second protomer. Left, top down view of the helices in the structural model; right, helical wheel diagram of the top two helical turns in the DHp dom ain; residues that form crosslinks are highlighted as before.

137 detection by Western blot analysis. BceS contains three native Cys residues, C45 in the
138 second transmembrane helix and C198 and C259 in the ATPase domain. Based on their
139 physical distance from each other and the DHp domain, we did not expect these residues to
140 interfere with our analysis, and indeed no crosslinking product was observed upon oxidation
141 with iodine in wild-type BceS (Fig. 2b). Next, single cysteine substitutions were introduced
142 in the first two helical turns of the helix DHp1 (N114 to M120), and in equivalent positions
143 near the end of the helix DHp2 (Q166 to R168). Disulfide bond formation in these variants
144 should only occur if the substituted residues come into close proximity in the kinase dimer [27].
145 The only residues that consistently formed detectable crosslinks were at positions 115, 118
146 and 119, with the highest degree of crosslinking at position 115 (Fig. 2b). This is in good
147 agreement with their positioning at the core of the four-helix bundle and shows that the
148 structural model closely reflects the conformation of BceS in the cell (Fig. 2c).

149 To ensure that the introduction of cysteines had not affected the integrity of the protein, we
150 tested the activity of each BceS variant *in vivo*. This was based on their ability to induce
151 expression from the system's target promoter fused to a reporter gene (P_{bceA}-*luxABCDE* or
152 P_{bceA}-*lacZ*), following exposure to the antibiotic bacitracin [1]. Only the K116C and K167C
153 substitutions led to a complete loss of activity (Fig. S1a). It is therefore possible that the lack
154 of crosslinking observed for the latter, which also faces the core of the DHp domain (Fig. 2c),
155 could be explained by defects in the protein rather than the distance between DHp2 helices in
156 the kinase dimer. However, the majority of BceS variants retained at least partial signaling
157 activity, confirming structural integrity of the kinase during the crosslinking analyses.

158 **Charge substitutions in the DHp core suggest a rotation mechanism of kinase**
159 **activation.** Closer inspection of the DHp domain revealed a striking concentration of charged
160 residues at the membrane-proximal end of the four-helix bundle (Fig. 3). In the wild-type

161 kinase, E115 and K167 create a net neutral charge in the bundle core. As described above and
162 previously [1], cells harbouring wild-type BceS strongly activate expression of the P_{bceA}-*lux*
163 reporter in the presence of bacitracin, while in the absence of the antibiotic the activity of the
164 reporter is below the detection limit (Fig. 3a, WT). Interestingly, creation of an 'all negative'
165 (K167D substitution) or 'all positive' (E115K substitution) DHp core resulted in a massive
166 increase in the basal level of the kinase, while the activity in the presence of the inducer
167 remained unaffected (Fig. 3a). To test whether this effect was indeed due to the changes in
168 core charge and not to substitutions at this position *per se*, we introduced a series of other
169 amino acids into position 115. Exchanging E115 for a different positively charged amino
170 acid, Arg, again resulted in an increase in basal activity, although less pronounced (Fig. S1c).
171 Substitution for Ala or Cys had no detectable effect on activity, showing that the presence of
172 charged amino acids was not in itself important for kinase function. Moreover, the
173 constitutive kinase activity could be returned to near wild-type levels by restoring the net
174 neutral charge through combining the E115K and K167D substitutions (Fig. 3a). We
175 therefore concluded that the high constitutive activity in the absence of the inducer was
176 indeed due to the presence of four residues with the same charge in the DHp domain core.

177 In the current model for histidine kinase activation, the DHp domain undergoes a helical
178 rotation [15]. The strong activating effect we observed upon introduction of four residues of the
179 same charge at the core of the domain made it tempting to speculate that charge repulsion
180 may force BceS to undergo such a rotating motion, placing it in its activated state. According
181 to our homology model, rotation of the helix DHp1 in a counter-clockwise direction and
182 DHp2 in clockwise should create two new points of contact between charged residues: point I
183 between E118 and K167, and point II between K116 and R168 (Fig. 3b). The opposing
184 charges in point I should have a stabilizing effect on the rotated state, and removing this in
185 the K167D variant may explain its lower basal activity compared to E115K (Fig. 3a). In

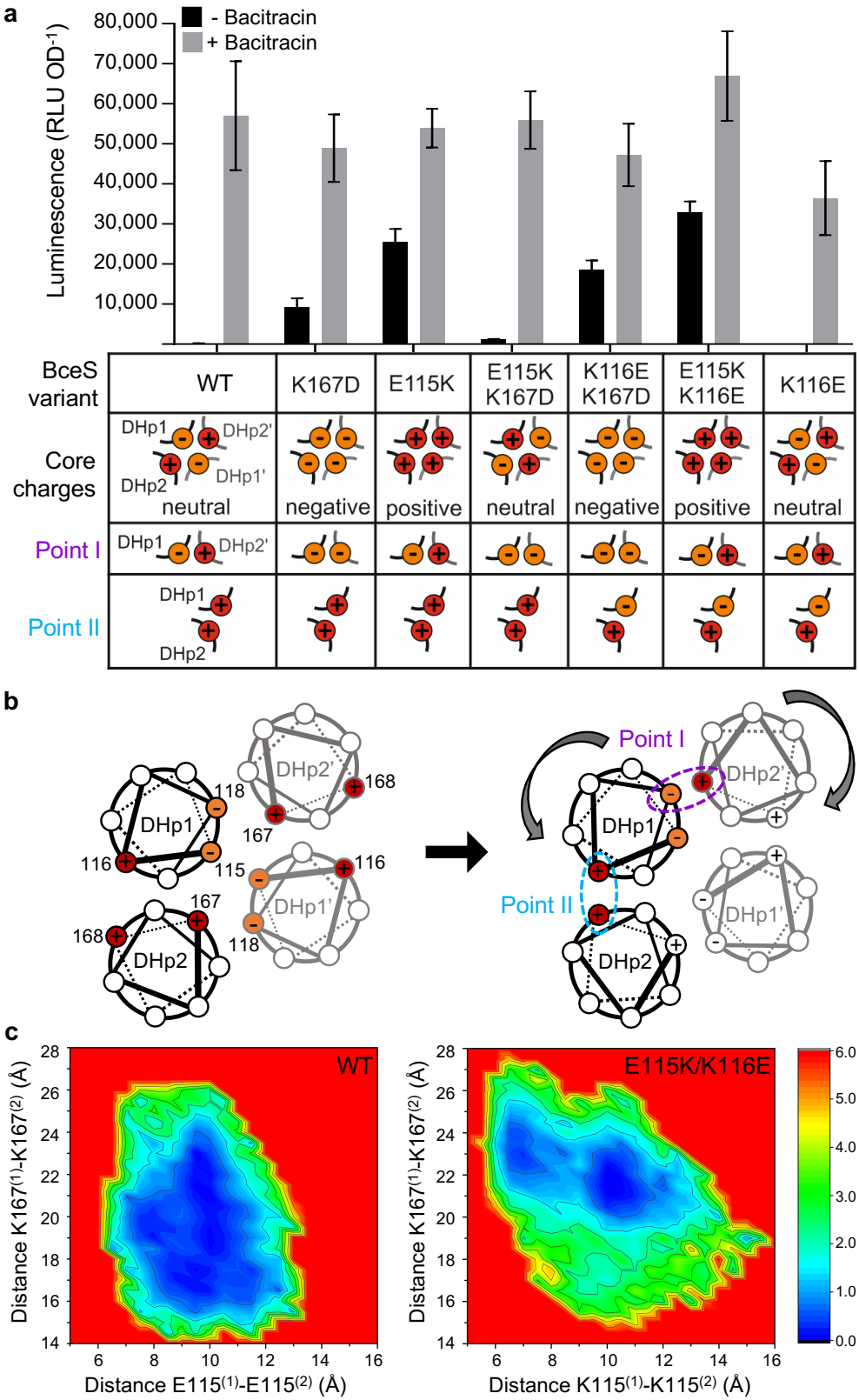

Figure 3: Charges within the BceS DHp domain core affect kinase activity. a, BceS signaling activity in strains harbouring P_{bceA}-*luxABCDE* and P_{xyl}-*bceS*. Amino acid substitutions were introduced in parent construct *bceS*^{WT}-His$_8$ (SGB369). Signaling was induced with 1µg ml^{-1} of bacitracin. Data are shown as mean ± SD from 4-22 biological repeats. The schematic below shows the location of individual and net charges in the core and stabilisation points within the four-helix bundle, as illustrated in panel b. Red, positive charge; orange, negative charge. **b**, Helical wheel diagram of the top two helical turns in the DHp dimer configuration showing location of charges and stabilisation points (pink and cyan). Helices labelled DHp1' and DHp2' show the second protomer. Black curve arrows denote the direction of helical rotation. **c**, 2D plots of potential of mean force (PMF) obtained in GaMD simulations of the wild type (WT, left) and E115K/K116E variant (right) protein. Inter-monomer distances shown are between the Cα carbon atoms of residues at positions 115 (x-axes) and 167 (y-axes). The PMFs are projected onto the surface in kcal mol^{-1} indicated by the heat scale.

186 contrast, the proximity of two positive charges in point II should have a de-stabilizing effect.
187 Replacing one of these with a negative charge (K116E) by itself had no effect on kinase
188 activity. However, combining K116E with the activating effect of the E115K substitution led
189 to a further increase of basal kinase activity compared to E115K alone (Fig. 3a). This effect is
190 entirely consistent with kinase activation through helical rotations in the DHp domain, where
191 we could achieve the highest artificial activation of the protein through creating charge
192 repulsion in the kinase core, while stabilizing the rotated state through opposing charges in
193 the two new points of contact.

194 Attempts were made to detect this DHp domain rotation *in vivo* using cysteine crosslinking,
195 either following induction with bacitracin or using the constitutively active E115K/K116E
196 variant. No quantitative conclusions could be drawn, however, due to the very large
197 experimental errors (Fig. S2). To provide further evidence of conformational change in the
198 DHp domain, we turned to molecular dynamics (MD) simulations. As discussed above, the
199 homology model (Fig. 2) shows excellent agreement with experimental validation, indicating
200 that it is a reasonable starting point for MD simulations. Given the relatively large putative
201 rotation, we applied Gaussian accelerated MD (GaMD) to more completely sample
202 conformational space. This approach applies a harmonic boost potential to effectively
203 'flatten' the free energy landscape, thereby enhancing the conformational sampling achieved
204 during MD simulation [28].

205 To assess conformational differences in the DHp domain between the wild-type kinase and
206 the constitutively active E115K/K116E variant, GaMD simulations were performed on both
207 for a total of 2 μs each (four replicas of 500 ns; Figure S3a). From our simulations, we
208 calculated the potential of mean force (PMF) for a series of internuclear distances for both
209 wild-type and variant residues. These values can serve as a proxy for the energetic barrier

210 between conformational sub-states. To best illustrate the relative orientation of helices in the
211 DHp domain bundle, we focused on positions 115 and 167, facing the bundle core (Fig. 3).
212 The PMF plots for the internuclear pairs of these residues between monomeric units of the
213 DHp domain are shown in Figure 3c. The lower the PMF value, the more likely the helices
214 will occupy the conformational state defined by the internuclear distances shown. In the wild-
215 type DHp domain, the PMF plot for distances between monomers at amino acids 115 and 167
216 shows a broad minimum across most of conformational space (Fig. 3c, left). This suggest that
217 there is a relatively high propensity for the domain to explore a diversity of conformational
218 space. Figure 3c (right) shows the same data for the variant DHp. Instead of the broad
219 minimum that characterizes the wild-type domain, the variant now shows two distinct, more
220 restricted minima. More specifically, the tendency towards a longer K167 distance in the
221 variant DHp would seem consistent with our model for helix rotation (Figure 3b). To more
222 clearly explore the differences between conformational space accessed by the wild-type and
223 variant DHp domain, we performed principal components analysis (PCA) of the data from
224 Figure 3c. This indicates that there is a significant difference in the principal component
225 space sampled by the wild-type and variant DHp (Fig. S3b). That is, the variant DHp
226 occupies a conformational space that is not accessible to the wild-type domain. Based on the
227 high constitutive activity of the variant, it is plausible to assume that this new conformational
228 space represents the active state of the kinase. Importantly, our simulations show that the
229 wild-type kinase is unable to adopt this conformation on the simulated time scales. This is
230 consistent with our *in vivo* experimental data that shows no detectable kinase activity without
231 activation through the sensory transporter BceAB.

232 **BceS contains a HAMP-like signal transfer domain.** Contrary to previous predictions, the
233 BceS homology model showed a domain with structural similarity to a HAMP domain
234 between the second transmembrane helix and the DHp domain. HAMP domains adopt a

235 parallel four-helix bundle arrangement with two alternative states of helix packing that
236 transmit a conformational change from an upstream input to a downstream output domain
237 [15,29,30]. While there is some argument over the exact motions within HAMP domains, there
238 seems to be agreement that they turn multiple input movements consistently into a helical
239 rotation [15,30]). The four-helix bundle is stabilized through multiple packing layers, forming
240 both inter- and intramolecular interactions, predominantly mediated by hydrophobic residues
241 [30,31]. A protein sequence alignment of known HAMP domains and the HAMP-like domain of
242 BceS is shown in Fig. 4a, with the positions of the critical packing points highlighted. The
243 hydrophobicity at these positions is largely conserved in BceS.

244 Previous investigations of HAMP domains have highlighted one particular residue with key
245 influence on the signaling state. This residue corresponds to L67 in BceS, a position most
246 commonly occupied by small hydrophobic residues that favour bundle packing (A or V,
247 occasionally I, L; Fig. 4a, black arrow) [30]. Based on extensive structural work on the HAMP
248 domain of the *A. fulgidus* protein Af1503, this residue (A291 in Af1503) has a crucial role in
249 controlling the conformational state of the HAMP domain. Specifically, it is thought that
250 increasing residue size at this position decreases the threshold for conversion between
251 packing states of the HAMP domain [30,32]. In Af1503, larger residues at this position increased
252 the signal responsiveness of a hybrid Tsr-HAMP-adenylate cyclase protein or of the HAMP-
253 EnvZ chimera our BceS homology model is most similar to [32,33]. Similarly, increasing the
254 size of the corresponding amino acid (V228I) in the HAMP domain of the histidine kinase
255 PhoQ of *Salmonella enterica* serovar Typhimurium led to elevated activity of the kinase,
256 while decreasing residue size had the opposite effect and reduced the PhoQ response to signal
257 [34].

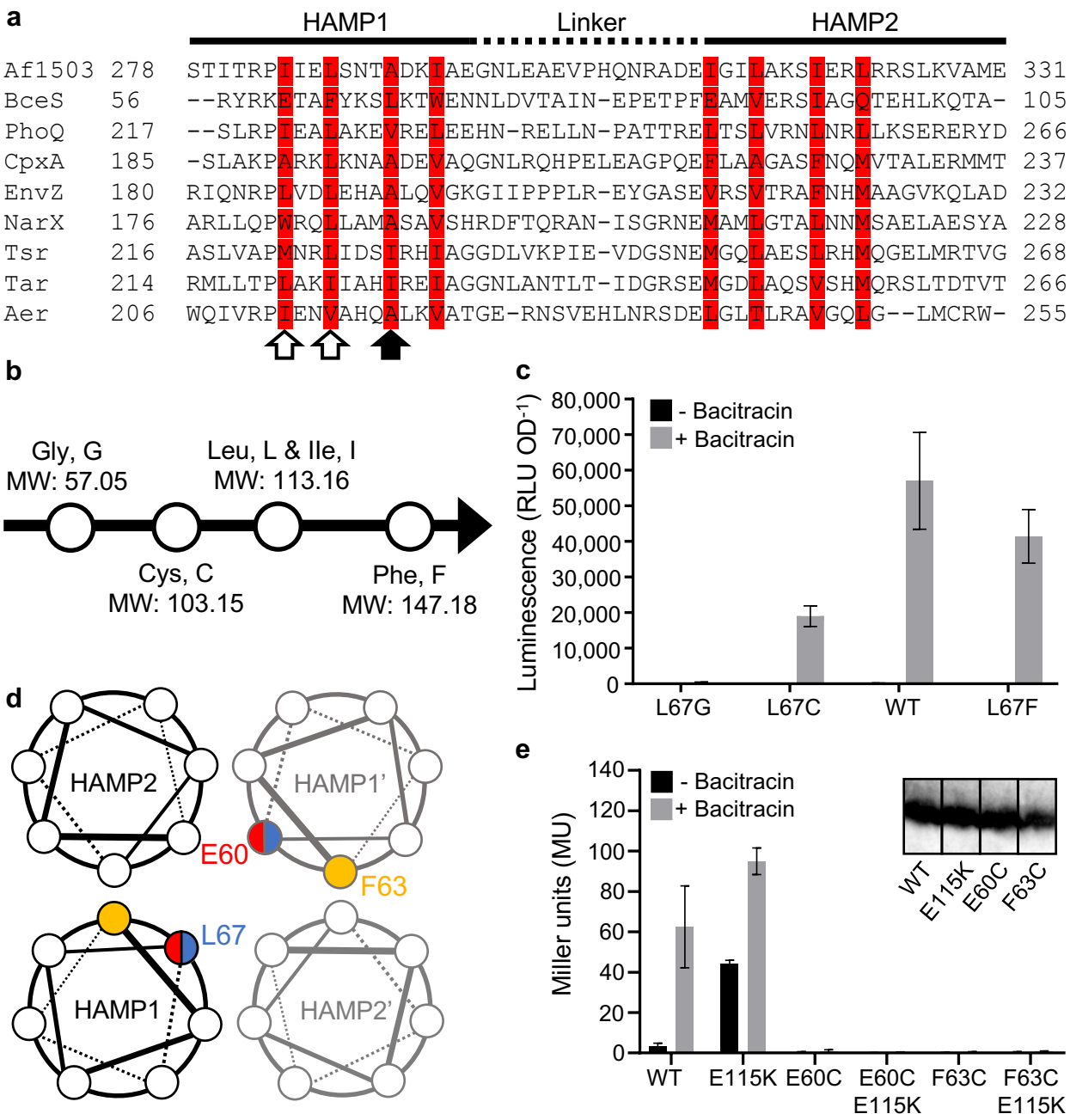

Figure 4: BceS contains a HAMP-like signal transfer. a, Sequence alignment of known HAMP domains and the BceS HAMP-like domain generated with ClustalO. Residues in red form the packing layers in the Af1503 HAMP domain. The black solid arrow indicates the packing residue that influences signaling state in some HAMP domains. White open arrows indicate E60 and F63 critical for BceS function. Proteins included and their GenBank identifiers are Af1503 (O28769), BceS (BSU30390), PhoQ (P23837), CpxA (P0AE82), EnvZ (P0AEJ4), NarX (P0AFA2), Tsr (P02942), Tar (P07017), Aer (P50466). **b**, Schematic showing amino acids and their sizes in MW used in size substitutions. **c**, BceS signaling activity following L67 amino acid size substitution harbouring P_{bceA}-*luxABCDE* and P_{xyl}-*bceS*. Amino acid substitutions were introduced in the parent construct *bceS*^{WT}-His$_8$ (SGB369). Signaling was induced with 1µg ml^{-1} of bacitracin. Data are shown as mean ± SD from 5-18 biological repeats. **d**, Helical wheel diagram of the HAMP-like domain. Helices labelled HAMP1' and HAMP2' show the second protomer . Residues essential for BceS activity are E60 (red) and F63 (yellow); the key packing residue L67 is shown in blue; red/blue semicircles are used to indicate positioning of residues in subsequent helical layers. **e**, BceS signaling activity of the constitutive ON variant (BceS^{E115K}) combined with loss-of-function substitutions at positions 60 and 63. Amino acid substitutions were introduced in parent construct *bceS*^{WT}-His$_8$ (SGB401). Signaling in cells harbouring P_{bceA}-*lacZ* and P_{xyl}-*bceS* was induced with 1µg ml^{-1} of bacitracin, BceS production was controlled by addition of 0.02 % (w/v) xylose. Data are shown as mean ± SD from 3-7 biological repeats. The inset shows an anti-His Western blot analysis to confirm membrane localisation and protein levels of wild-type (WT) BceS and its variants.

258 To test if the HAMP-like domain discovered in BceS fulfils an equivalent function to other
259 HAMP domains, we therefore investigated the role of amino acid size at this position by
260 changing L67 to the smaller Gly and Cys, as well as the larger Phe side chain (Fig. 4b).
261 Indeed, smaller size substitutions reduced BceS activity, up to a near-complete loss of
262 induction in the Gly variant (Fig. 4c). Increasing the size to Phe, however, did not lead to an
263 increase of signaling nor changed the basal activity of BceS. Our data are thus consistent with
264 the notion that small residues at this position may increase the threshold for conversion
265 between HAMP-domain conformations [30,32], but we could not find a stimulating effect
266 through a larger residue. The latter was also found in *E. coli* NarX, where an A189V
267 substitution at the equivalent position to L67 in BceS led to a decrease of signal output [35].
268 The precise effect of changing this residue may therefore depend on the specific context in
269 different protein. We nevertheless conclude from our data that the HAMP-like domain in
270 BceS appears to be a functional equivalent to conventional HAMP domains in other proteins
271 and likely contributes to signal transfer within the histidine kinase.

272 For further functional investigation, we carried out Cys scanning mutagenesis of both helices
273 within the HAMP-like domain. The majority of variants maintained at least partial signaling
274 activity (Fig. S4), and in contrast to other studies [34,35], we did not find any substitutions that
275 led to a constitutively active state of BceS. The only two substitutions that caused a complete
276 loss of function were E60C and F63C (Fig. 4 and S4). Interestingly, these fall on the first two
277 positions of the packing motif (Fig. 4a, white arrows and 4d), with E60 located one packing
278 layer above the critical L67 discussed earlier, and are therefore likely of structural
279 importance. Both variant proteins are present in the cytoplasmic membrane at the same levels
280 as the wild type protein according to Western blot analysis (Fig. 4e inset), showing that the
281 lack of signaling is not caused by general protein misfolding. To test if the defect of the two
282 variants was due to a loss of signal transfer from either the TM region of the protein or the

283 transporter, we combined each of the LOF mutations with the E115K substitution that
284 activates BceS in the absence of a stimulus. All resulting variants remained completely
285 inactive (Fig. 4e), which showed that the substitutions in the HAMP-like domain had a
286 dominant effect and thus likely caused substantial structural disruptions in the protein, rather
287 than specifically affecting signal transfer.

288 **Activation of BceS involves a piston-like displacement in transmembrane helix 2.** We
289 next investigated the conformation of the second transmembrane helix in BceS. In many
290 histidine kinases, conformational changes in an extracellular sensory domain upon ligand
291 binding or signal perception are transmitted to the cytoplasmic region of the protein through
292 physical movement of the intervening transmembrane helix [14]. In the case of BceS, however,
293 signaling is entirely reliant on the BceAB transport system and therefore does not involve
294 canonical transmembrane information transfer. To investigate if BceS activation nevertheless
295 involved transmembrane helix movements, we carried out a cysteine accessibility scan (Scan-
296 SCAM, [18]) of its second transmembrane helix. This analysis requires a cysteine-free
297 background, and we therefore replaced the three native Cys residues mentioned earlier by
298 serine. The C45S/C198S/C259S BceS variant showed comparable signaling activity to the
299 wild-type kinase and was therefore deemed fully functional (Fig. S5). Transmembrane
300 topology predictions of BceS place the membrane interface approximately at residues W54 or
301 F55. We therefore individually replaced each residue from positions 51 to 65 with Cys, with
302 the exception of E60 and F63, which were essential for BceS activity (see above). Again,
303 none of the resulting variants showed any defects in signaling (Fig. S5). The position relative
304 to the membrane was then tested for each Cys residue based on its solvent accessibility, using
305 a modified version of the established *E. coli* protocol [18]. In brief, treatment of whole cells
306 with N-ethyl-maleimide (NEM) should block any solvent-exposed Cys residue through
307 reaction with the sulfhydryl group, whereas in untreated cells these groups should remain

308 available for later reactions. Following isolation of membranes, any unblocked Cys residues
309 are then reacted with methoxypolyethylene glycol maleimide (PEG-mal), resulting in a 10
310 kDa increase in size, detectable by Western Blot analysis. For cytoplasmic Cys residues in
311 BceS, we therefore expected to see a shift in size only in samples that had not been treated
312 with NEM (Fig. 5, blue labels). In the established methodology used for *E. coli*, membrane-
313 embedded Cys residues are protected by their membrane environment from blocking by
314 NEM, but become available for PEGylation upon solubilisation in SDS [18]. However, in *B.*
315 *subtilis* membranes we could not observe PEGylation of membrane-embedded Cys residues
316 regardless of the presence of SDS, possibly due to differences in membrane composition. We
317 therefore interpreted those residues as being membrane embedded that did not show a size
318 shift in either presence or absence of NEM treatment (Fig. 5, red labels). The results from the
319 Scan-SCAM analysis showed that residues up to position 56 resided in the solvent-
320 inaccessible membrane environment, while residues from Y57 onwards were accessible and
321 therefore cytoplasmic (Fig. 5, 'OFF state'). The apparent inaccessibility of Y64 was
322 disregarded based on its distance from the likely membrane interface. We then repeated the
323 same analysis in the background of the E115K/K116E substitutions that place the kinase in a
324 constitutively active conformation. Here, residues from F55 onwards became consistently
325 solvent-accessible (Fig. 5, 'ON state'). Comparison of the two states therefore shows that
326 BceS activation involved an inward piston-like displacement by two amino acids of the
327 second transmembrane helix.

328 We next sought to test whether BceS could be activated by artificially inducing a shift
329 through introduction of arginine residues near the membrane interface. Due to their positive
330 charge, Arg residues prefer to move towards a hydrophilic environment. When introduced in
331 a transmembrane segment, this can induce a shift towards the nearest solvent interface, which
332 has been shown to cause signal-independent activation of the *E. coli* histidine kinase DcuS [18].

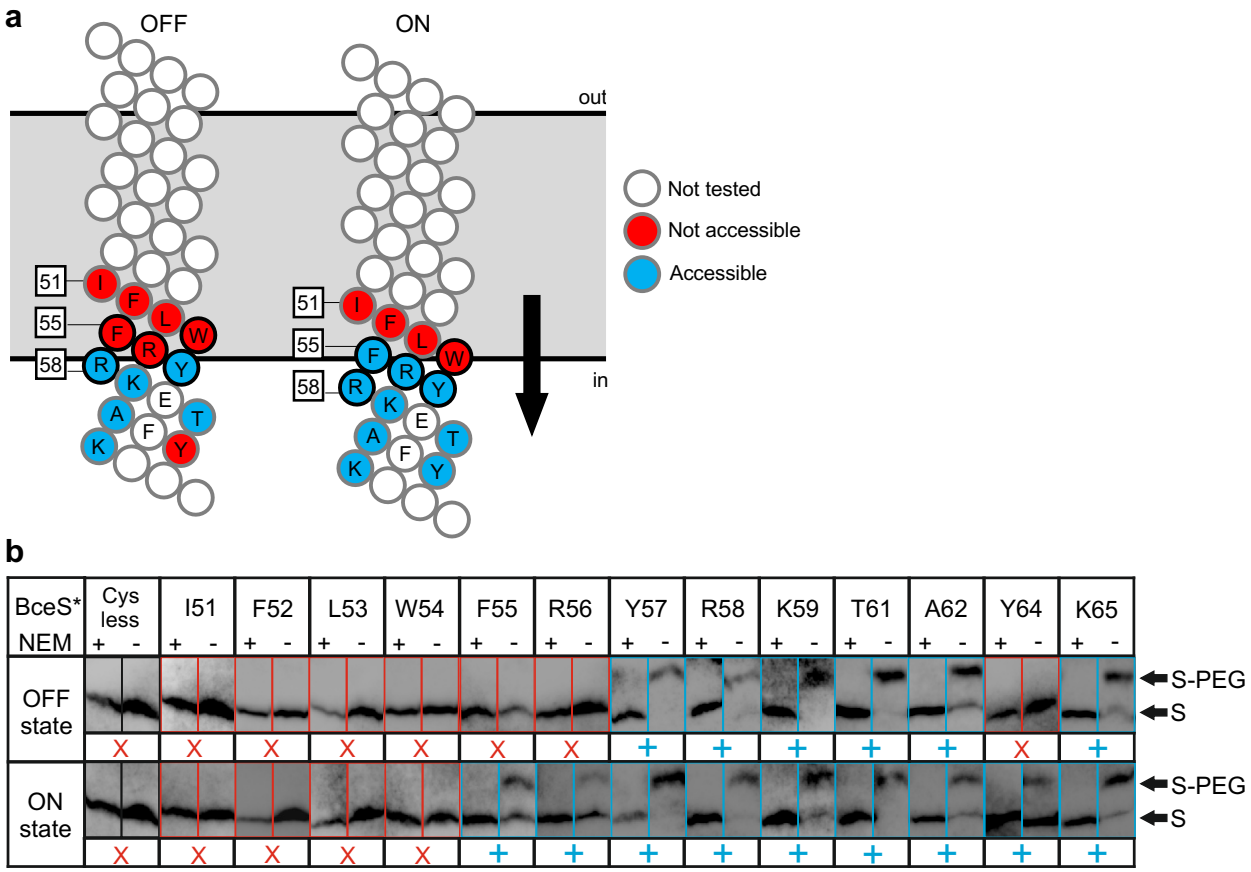

Figure 5: Accessibility of Cys residues at the membrane interface shows a piston-like displacement upon BceS activation. a, Schematic representation of transmembrane helix 2 in the OFF and ON states, respectively. Relevant native amino acids are indicated in one-letter code. Solvent-accessible (PEGylated) Cys replacements are shown in blue, inaccessible (unPEGylated) Cys replacements in red and residues not tested in white. Residues circled in black were tested in triplicate, those circled in grey in duplicate. **b**, Anti-His Western blot analysis of solvent-accessibility of Cys replacements (Scan-SCAM). Bands corresponding to PEGylated (S-PEG) and unmodified (S) BceS are indicated; individual lanes are outlined in the same colour code as used in panel a. 'Cys-less' indicates the parent variant of BceS lacking its native Cys residues. OFF state: amino acids substituted in parent construct *bceS*$^{C45S/C198S/C259S}$-His$_8$ (SGB936). ON state: amino acids substituted in parent construct *bceS*$^{E115K/K116E/C45S/C198S/C259S}$-His$_8$ (SGB951).

333 We therefore substituted three of the residues near the cytoplasmic end of transmembrane
334 helix 2 of BceS (W54, F55 and Y57) with Arg, individually and in pairs. (Fig. S6). Variants
335 containing the W54R substitution had approximately 60% higher activities upon stimulation
336 with bacitracin (Fig. S6), which may indicate a stabilisation of or lowered transition threshold
337 to the activated state. However, none of the variants showed a detectable change of basal
338 activity in the presence or absence of the input transporter BceAB, leading us to conclude
339 that Arg substitution alone was not sufficient to activate the kinase, which still relied on
340 BceAB for signaling.

341 **The transporter BceAB has complete control over kinase conformation**. It was
342 previously shown for Bce of *B. subtilis* and several other examples of the same type of
343 resistance system that activation of signaling is completely reliant on the ABC transporter
344 [3,4,7,8,24]. We further showed through computational modelling that the signaling output via
345 BceS is directly proportional to the activity of BceAB and does not follow the switch-like
346 on/off behaviour seen in most other systems using transporters as accessory sensing proteins
347 [1,20]. This led us to hypothesise that BceAB completely controls the conformation of BceS and
348 thus slaves kinase activity directly to its own transport activity. Our discovery of the DHp
349 domain variants that cause artificial activation of BceS now for the first time enabled us to
350 test this hypothesis experimentally by investigating the role of BceAB in controlling the OFF
351 state of the kinase.

352 In cells harbouring the wild-type sequence of BceS, the OFF-state activity in un-stimulated
353 cells is below the detection limit of our assays, and deletion of the transporter therefore has
354 no measurable effect (Fig. 6a). However, in the E115K or the E115K/K116E variants, basal
355 kinase activity was high, allowing us to test the effect of *bceAB* deletion in the absence of
356 bacitracin. Removing the transporter in this background caused a striking further increase in

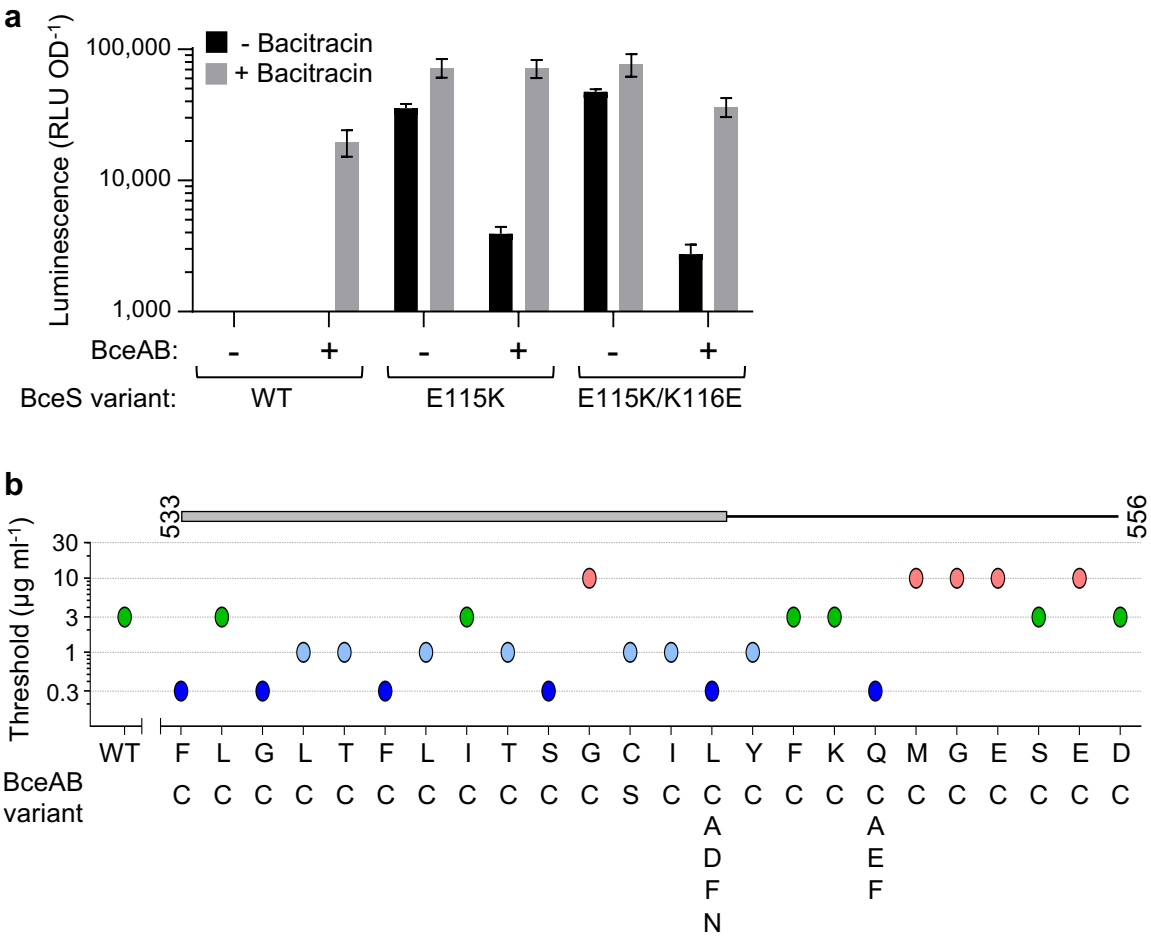

Figure 6: Control of BceS activity by the transporter BceAB. a, Signaling activity of BceS measured in strains harbouring P_{bceA}-*luxABCDE* and challenged with 10µg ml^{-1} of bacitracin (grey) or left untreated (black). Amino acid substitutions were introduced into parent construct P_{xyl}-*bceS*-His_8, in a strain background carrying a Δ*bceS* deletion (BceAB +; SGB792), or a Δ*bceSAB* deletion (BceAB -; SGB818). Data are shown as mean ± SD from 5-12 biological repeats. **b,** Signaling phenotype of BceAB variants. Amino acid substitutions were introduced into the P_{xyl}-*bceAB*-$FLAG_3$ parent construct, and signaling assessed using either a P_{bceA}-*lacZ* (SGB370 and derivatives) or P_{bceA}-*luxABCDE* (SGB731 and derivatives) reporter. Cells were challenged with a series of bacitracin concentrations, and the lowest concentration giving signaling above background is shown by circles in the plot (see Fig. S7 for complete datasets). Analyses were based on mean values from at least three independent repeats. The first line of x-axis labels gives native amino acids, the lines below indicate substitutions tested. The bar above the graph shows positions in the BceB sequence and areas within the membrane (grey bar) or in the cytoplasm (black line). Circle colours are assigned green, wild-type (WT) signaling threshold; red, increased signaling threshold; blue, reduced signaling threshold.

357 activity, rendering the kinase fully activated irrespective of the presence of the inducing
358 antibiotic (Fig. 6a). This shows that in the absence of its substrate bacitracin, the inactive
359 transporter can inhibit the activity of the constitutively active DHp domain variants, which
360 manifests as an approximately ten-fold reduction in basal activity compared to the
361 transporter-free state. Our data are therefore consistent with a model where inactive BceAB
362 exerts close control over BceS keeping the kinase in its inactive state. This reveals a further
363 layer of kinase control in addition to the transporter's known activating effect in the presence
364 of the antibiotic [1].

365 **BceAB has not evolved for maximal signaling sensitivity.** Recent structural biology work
366 has provided new insights into the functional mechanism of the Type VII superfamily of
367 ABC transporters, of which BceAB is a member. This group of proteins, exemplified by
368 MacB of *E. coli*, is thought to act as mechanotransmitters, using cytoplasmic ATP hydrolysis
369 to provide energy for periplasmic processes, such as removal of antibiotics [36]. In MacB,
370 mechanotransmission is achieved by the transmembrane helix linking the cytoplasmic
371 ATPase interaction site to the periplasmic domain [36]. In BceAB, the equivalent region is its
372 eighth transmembrane helix, which connects the transporter's extracellular domain to a
373 cytoplasmic loop containing one of the ATPase contact interfaces (Fig. 1) [11]. Strikingly, in a
374 previous random mutagenesis analysis we had discovered that this region of BceB contained
375 a particularly high density of mutations leading to a loss of signaling [37]. It was therefore
376 tempting to speculate that this region was crucial for the communication between transporter
377 and kinase. To investigate this further, we carried out another Cys scan, individually
378 replacing each residue from positions 533 to 556 in BceB, encompassing approximately half
379 of transmembrane helix 8 and the first alpha-helical segment of the adjacent cytoplasmic
380 region. The native Cys at position 544 was replaced by Ser. The resulting variants were tested
381 for their ability to complement a *bceAB* deletion strain for signaling and resistance activities.

382 With the exception of the strain harbouring the G535C variant, all displayed comparable
383 bacitracin resistance to the control containing the wild-type sequence of *bceAB* on the same
384 genetic construct (Table S4), showing that the resulting transporters were fully functional.
385 Signaling was tested using our standard reporter gene assays (P_{bceA}-*luxABCDE* or P_{bceA}-*lacZ*).
386 All variants except G543C reached a similar amplitude of reporter induction as strains
387 containing the wild-type construct (Fig. S7 a&b). However, we observed some clear
388 difference in the sensitivity of signaling, i.e. the minimal concentration of antibiotic required
389 to elicit a response. In cells with the wild-type construct, the lowest bacitracin concentration
390 to trigger signaling was 3 μg ml^{-1}, while a number of variants had a higher threshold of 10 μg
391 ml^{-1} (Fig. 6b, green vs red dots; Fig. S7 a&b). The majority of these fell into the C-terminal
392 part of the scanned region, indicating potential defects in coupling to the ATPase. To our
393 surprise, we also found several variants that showed a marked increase in signaling
394 sensitivity and responded already at 0.3 μg ml^{-1} or even 0.03 μg ml^{-1} bacitracin (Fig. 6b, dark
395 blue dots; Fig. S7). We had previously seen that a reduction of BceAB transport activity can
396 cause such a shift in signaling threshold, because the negative feedback created by removal of
397 the antibiotic is missing [1]. However, as none of these variants showed any change in
398 bacitracin resistance (Table S4), loss of antibiotic removal cannot explain the increased
399 signaling sensitivity. Mapping of these residues showed that they occurred with a regular
400 periodicity of every four amino acids (Fig. 6b), suggesting they are positioned along the same
401 face of the transmembrane helix. Figure S7c shows a homology model from I-TASSER of
402 the final three transmembrane helices of BceB, for which MacB was the closest structural
403 analog, to illustrate the potential arrangement of these residues. Substitutions with the
404 relatively small amino acid Cys may have enabled tighter helix packing, potentially
405 contributing to more effective signaling. To test this, we replaced two of the positions, L546
406 and Q550, with a series of other amino acids, including small Ala; charged Glu or Asp; and

407 large Phe. Regardless of the substitution made, deviation from the wild-type sequence at
408 these positions consistently led to an increase in signaling sensitivity (Fig. 6b). It is difficult
409 to envisage that all these substitutions caused tighter interactions with the kinase. An
410 alternative explanation may be that they are involved in tightly coupling ligand binding by
411 the extracellular domain to ATP hydrolysis, and that substitutions weaken this coupling,
412 allowing ATP hydrolysis and therefore signaling to occur at lower substrate concentrations. It
413 is beyond the scope of this study to investigate the mechanistic details of the transporter
414 further to answer this question. However, our findings clearly show that the transporter
415 contains a series of residues that likely form a continuous face on transmembrane helix 8,
416 which prevent signaling from occurring at lower bacitracin concentrations. Given that any
417 replacement we tested led to more sensitive signaling, we therefore conclude that the
418 transporter has evolved to avoid hyper-sensitive signaling, and that this likely constitutes a
419 further layer in minimizing the fitness cost of resistance.

420 **DISCUSSION**

421 In this study, we set out to investigate the molecular mechanisms of the flux-sensing strategy
422 employed by Bce-like antibiotic resistance systems. Their hallmark feature is that histidine
423 kinase activity not only fully depends on the presence of its cognate transporter, but is
424 directly proportional to transport activity across a large input dynamic range of antibiotic
425 concentrations [1]. This careful adaptation of signaling activity ensures the resistance
426 transporter is produced precisely to the cell's demand for detoxification capacity, a very cost-
427 efficient strategy to control gene expression. The results presented here now provide
428 molecular level understanding of how such close control over kinase activity, implementing
429 regulation akin to an analog dial, can be achieved.

430 Analyses of BceS conformation in the inactive and active state showed a piston-like inward
431 displacement of the second transmembrane helix and helical rotation within the DHp domain
432 upon kinase activation. The intervening linker region is not sufficiently conserved in
433 sequence for *in silico* identification of any specific domains. However, tertiary structure
434 predictions and experimental validation indicate that BceS possesses a HAMP-like domain
435 that likely fulfils the signal transfer function. Based on crystallographic evidence from a
436 truncated kinase, it has been proposed that in HAMP-containing histidine kinases ligand
437 binding typically induces piston-displacements in the membrane, and these are converted by
438 the HAMP domain into rotational motion of the DHp domain [15]. Kinases without a HAMP
439 domain instead directly experience rotational motions in their transmembrane segments upon
440 ligand binding [15]. Despite its unusual input mechanism via the BceAB transporter, the
441 conformational changes we observed within BceS are therefore consistent with this proposed
442 mode of activation of HAMP-containing histidine kinases.

443 A recent NMR study reported on the structure of the BceS-like kinase NsaS from *S. aureus*,
444 which possesses a much shorter linker region between its transmembrane and DHp domains.
445 This linker region adopts a coiled-coil conformation instead of the HAMP-like fold of BceS
446 [17]. Inspection of kinase sequences in an existing collection of Bce-like resistance systems [5]
447 showed that the vast majority of these proteins contained the larger version of the linker
448 (approximately 60 amino acids), and only a small number possessed short (around 20 amino
449 acid) linkers with a predicted coiled-coil motif. BceS therefore appears to be the more typical
450 subtype of this group of kinases than NsaS. Interestingly however, akin to the alternative
451 helix packing mechanism proposed for HAMP domains [30], activation of NsaS was also
452 proposed to involve switching between helical packing states of the coiled-coil [17]. The
453 molecular principles of activation may therefore be conserved between both subtypes of
454 BceS-like kinases.

455 To further investigate the activation mechanism of BceS, we sought to force each of the
456 conformational changes via amino acid substitutions. Introduction of residues with the same
457 charge at the core of the DHp domain to cause helical rotation consistently led to kinase
458 activation without the need for the physiological stimulus (Fig. 3). However, we were unable
459 to artificially trigger activation through substitutions that should have induced piston
460 displacements in the membrane (Fig. S6) or induced the active conformation of the HAMP
461 domain (Fig. 4 and S4). This is in contrast to studies of other kinases where such
462 substitutions were able to at least partially raise the basal kinase activity [18,34,35]. In canonical
463 histidine kinases, the input signal is detected directly, e.g. through ligand binding. One could
464 therefore speculate that in these proteins, conformational changes have to be smoothly
465 transmitted from each domain to the next, and that this is reflected in the relative ease with
466 which kinase activity can be artificially induced through changes in each individual domain.
467 In contrast, BceS-like proteins are subject to control by the transporter. We do not yet know
468 with which part of the kinase the transporter interacts, although the transmembrane or
469 HAMP-like domains are the most likely. In a kinase that relies on such external control, it is
470 conceivable that small changes in upstream domains are insufficient to trigger rotation of the
471 DHp domain helices, and only manipulation of the DHp domain itself can cause artificial
472 activation. Some support for such a hypothesis may be found in the MD simulations. Our
473 analyses showed that the wild-type DHp domain does not by itself sample the conformational
474 space observed in the active variant (Fig. S3), implying that the transporter is likely required
475 to provide the necessary force for transition to the active state.

476 The use of transporters in accessory control of signaling proteins is not uncommon in
477 bacteria, but BceAB is unusual in that it is an activator of signaling, while most other
478 transporters act as repressors [20]. Repression of signaling and its relief are easily envisaged via
479 complex formation and dissociation between transporter and histidine kinase. For the Bce

480 system, we previously showed that transporter and kinase constitutively form a signaling
481 complex in the membrane, irrespective of the presence or absence of the inducer, bacitracin [2].
482 Considering its activating role and that signaling is proportional to transport activity, the
483 transporter must therefore be able to directly influence kinase activity within this complex.
484 When this was first tested *in vitro*, it was noted that BceAB had a negative effect on the
485 kinase autophosphorylation rate in the OFF state, although we could not explain the
486 observation at the time [2]. In the present study, we now show that the transporter indeed not
487 only controls the ON but also the OFF state of BceS *in vivo* and is able to restore partial
488 control over the high constitutive activity of the DHp domain variant (Fig. 6a). We propose
489 that through controlling both states of the kinase, the transporter is able to exert the level of
490 close control that is needed to explain the enormous dynamic range of the system, where
491 signaling is maintained in proportion to transport activity over more than three orders of
492 magnitude in antibiotic concentrations [1]. A crucial feature of the flux-sensing mechanism is
493 that signaling is immediately reduced if transport activity is low, either because the antibiotic
494 threat is over or because the cell has reached sufficient detoxification capacity [1]. Importantly,
495 the ability of BceAB to actively switch off BceS activity described here explains how this
496 energy-conserving signaling strategy is realized on the molecular level. Moreover, control
497 over the OFF state also allows the transporter to actively prevent any spurious signaling by
498 the two-component system in the absence of the antibiotic. Finally, our mutagenesis analysis
499 of BceAB revealed that the transporter itself has evolved to avoid signaling at very low
500 antibiotic concentrations, highlighting yet another level of cost reduction.

501 Taken together, we here present a molecular level model for activation of antibiotic
502 resistance based directly on the cell's need for protection, using a flux-sensing signaling
503 strategy that employs multiple layers of active energy conservation to minimize any fitness
504 costs of resistance. The system studied here is centered on two-component signaling, one of

505 the most important regulatory features of bacteria, and employs a histidine kinase of rather
506 typical domain composition. Our findings should therefore have wide relevance and serve as
507 a model for understanding, in general, how analog dials can control fine-tuned gene
508 expression in bacteria to achieve an optimal cost-benefit balance. In turn, the design
509 principles of an analog dial, we suggest, could usefully be employed in the context of
510 synthetic biology.

511 **METHODS**

512 **Bacterial strains and growth conditions.** All strains used in this study are listed in table S1
513 and were routinely grown in Lysogeny Broth (LB; 10 g l^{-1} tryptone, 5 g l^{-1} yeast extract, 5 g l^{-}
514 ^{1} NaCl) at 37 ºC with aeration. Solid media contained 15 g l^{-1} agar. Selective media contained
515 chloramphenicol (5 µg ml^{-1}), macrolide-lincosamide-streptogramin B (erythromycin; 1 µg
516 ml^{-1}, lincomycin; 25 µg ml^{-1}), spectinomycin (100 µg ml^{-1}), kanamycin (10 µg ml^{-1}), or
517 ampicillin (100 µg ml^{-1}).

518 **DNA manipulation and strain construction.** All primers and plasmids used in this study
519 are given in tables S2 and S3, respectively, with the use of each primer specified in table S3.
520 Site-directed mutagenesis was carried out according to the manufacturer's instructions for the
521 QuikChange II site-directed mutagenesis kit (Agilent Technologies), or by PCR-overlap
522 extension [38]. *Bacillus subtilis* transformations were carried out via natural competence as
523 previously described [39]. DNA for transformation was either provided as linearised plasmid
524 DNA, or as genomic DNA from a *B. subtilis* strain already carrying the desired genetic
525 construct.

526 To allow manipulation of both *bceS* and *bceAB* sequences, an unmarked deletion strain
527 lacking all three genes (Δ*bceSAB*, SGB377) was constructed as described previously [40],

528 employing plasmid pAK102. Strains lacking *bceS* only (Δ*bceS*; TMB1036) or *bceAB* only
529 (*bceAB*::kan; TMB035 [24]) were available from previous work. Signaling activity was
530 assessed in strains harbouring a chromosomally integrated transcriptional reporter construct
531 of the target promoter P_{bceA}, fused to either *luxABCDE* (pSDlux101 [37]) or *lacZ* (pER603 [24]).
532 Details of the assays used are given below.

533 Genetic manipulation of *bceS* was performed using previously constructed plasmids as
534 template. For Western blot detection, the construct pSD2E01 encoding BceS with a C-
535 terminal octa-histidine tag (P_{xyl}-*bceS*^{WT}-His_8 [2]) was employed. Un-tagged constructs were
536 derived from pAS719 (P_{xyl}-*bceS*^{WT}). Genetic manipulation of *bceAB* was performed using the
537 previously constructed plasmid pFK727, encoding BceAB with a C-terminal triple FLAG-tag
538 on the permease (P_{xyl}-*bceAB*-$FLAG_3$ [37]). All constructs used in this study integrate stably and
539 as a single copy into the *B. subtilis* W168 chromosome.

540 **Signaling activity assays.** In strains carrying the P_{bceA}-*lacZ* reporter, signaling was assessed
541 following challenge of exponentially growing cells with Zn^{2+}-bacitracin (bacitracin) and
542 measured as β-galactosidase activity (expressed in Miller Units), as described previously [24].
543 For strains carrying the P_{bceA}-*luxABCDE* reporter, luciferase activities were assayed using a
544 Tecan® Spark® microplate reader controlled by SparkControl™ V2.1 software. Starter
545 cultures were grown at 37 ºC in 2 ml of LB medium overnight, then diluted 1:1000 into fresh
546 medium before adding 100 µl into 96-well plates (black, clear flat bottoms; Corning®).
547 Samples were grown at 37 ˚C with orbital agitation at 180 rpm and allowed to achieve early
548 exponential growth (OD_{600} 0.3 – 0.4), before adding Zn^{2+}-bacitracin to a final concentration
549 of 1 µg ml^{-1} unless otherwise indicated. OD_{600} and relative luminescence units (RLU;
550 integration time 1 s) were measured every 5 min and were background-corrected using values

551 from LB-only wells. RLU was normalised for cell density (RLU OD^{-1}). The reported values
552 are steady-state activities achieved 60-75 min after bacitracin addition.

553 Cells were grown without the addition of xylose, as the basal activity of the promoter P_{xylA} [41],
554 used to drive expression of the ectopic copies of *bceS* and/or *bceAB*, was sufficient to achieve
555 full signaling activity. In strains containing the native copy of *bceAB* (Δ*bceS* background)
556 signaling was induced with 10 µg ml^{-1} of Zn^{2+}-bacitracin. In strains containing only the
557 ectopic construct for BceAB production (Δ*bceSAB* background), signaling was induced with
558 1 µg ml^{-1} of Zn^{2+}-bacitracin. These concentrations were established in our earlier work as
559 eliciting maximum signaling activity in the respective genetic backgrounds [1].

560 **Bacitracin sensitivity assays.** The sensitivity of *B. subtilis* strains to bacitracin was
561 determined as described [37], with minor modifications. Serial two-fold dilutions of Zn^{2+}-
562 bacitracin from 32 µg ml^{-1} to 0.5 µg ml^{-1} were prepared in Mueller-Hinton medium
563 containing 0.2 % (w/v) xylose to ensure maximal production of BceAB. For each
564 concentration, 100 µl volumes in 96-well plates were inoculated 1:400 from overnight
565 cultures grown in Mueller-Hinton medium with xylose and selective antibiotics. Each culture
566 was scored for growth after 20 to 24 h of incubation at 37°C with aeration. The MIC was
567 determined as the lowest bacitracin concentration where no visible growth was detected.

568 **Cysteine cross-linking *in vivo*.** Cysteine cross-linking was assessed in strains carrying the
569 Δ*bceSAB* deletion complemented with xylose-inducible ectopic copies of *bceAB*-$FLAG_3$ and
570 *bceS*-His_8 with single-cysteine substitutions and the P_{bceA}-*lux* reporter (SGB369 and
571 derivatives). Starter cultures were grown in 2 ml of LB medium overnight at 37 ºC with
572 agitation, then diluted 1:500 into 55 ml of fresh medium supplemented with 0.02% (w/v)
573 xylose. In mid-exponential growth (OD_{600} 0.5 – 0.7), oxidative cross-linking of cysteine
574 residues was triggered by addition of 250 µM of iodine for 15 min under continued

575 incubation. Where required, cells were induced with 60 µg ml^{-1} Zn^{2+}-bacitracin for 45 min
576 prior to cross-linking. Cross-linking reactions were stopped with 20 mM N-ethylmaleimide
577 (NEM) for 15 min under continued incubation. Cells were harvested by centrifugation (3,000
578 × *g*, 20 min, 4 ºC) and resuspended in 5 ml of ice cold lysis buffer (100 mM Tris-HCl [pH
579 8.0], 150 mM NaCl, 10% (w/v) glycerol, 20 mM NEM). Cell disruption was achieved by at
580 least three cycles of 15s sonication on ice with 15s rest. Debris was removed by
581 centrifugation (3,000 × *g*, 20 min, 4 ºC), and membranes were collected from supernatants by
582 ultracentrifugation (150,000 × *g*, 1 h, 4 ºC). Membranes were resuspended in 50 µl lysis
583 buffer, and approximately 150 mg protein per sample was mixed with non-reducing sample
584 buffer (1× final concentration; 1.5 M Tris/HCl [pH 6.8], 30 % (w/v) glycerol, 350 mM SDS,
585 0.12 mg ml^{-1} bromophenol blue) for SDS-PAGE and Western blot analysis (see below). For
586 quantification of band intensities Fiji [42] was used to obtain a profile plot of each lane, and the
587 relative intensity of each band (monomer and dimer BceS) within the lane was expressed as a
588 percentage of the total band intensities.

589 **Solvent-accessibility of Cysteine residues *in vivo* (Scan-SCAM).** For solvent-accessibility
590 tests in the second transmembrane helix of BceS, the Δ*bceSAB* deletion strain, complemented
591 with xylose-inducible ectopic copies of *bceAB*-$FLAG_3$ and *bceS*-His_8 and the P_{bceA}-*lux*
592 reporter was employed. The *bceS* complementation construct was made cysteine-free via
593 C45S/C198S/C259S substitutions, followed by introduction of single cysteines to be tested
594 (strain SGB936 and derivatives). The same was done in the E115K/K116E variant to assess
595 transmembrane topology in the active state (strain SGB951 and derivatives). Cultures were
596 grown to mid-exponential phase as described above. Cells were harvested, washed twice with
597 50 mM HEPES buffer (pH 6.8) and resuspended in 5 ml of the same buffer. Water exposed
598 (i.e. cytoplasmic) cysteine residues were masked with 40 mM N-Ethylmaleimide (NEM) for
599 1.5 h at room temperature with shaking or left untreated. Masking reactions were stopped by

600 three washes in cold (4 ˚C) 50 mM HEPES buffer (pH 6.8). Cells were resuspended in 5 ml
601 of ice cold lysis buffer, sonicated and membranes collected as above. Membranes were
602 resuspended in 40 µl accessibility buffer (50 mM HEPES [pH 6.8], 1.3% (w/v) SDS).
603 Cysteines that had not been masked with NEM in the first step were labelled with 5 mM
604 methoxypolyethylene glycol maleimide (PEG-mal; Sigma-Aldrich) for 1.5 h at room
605 temperature with agitation. The reaction was stopped with 1× LDS sample buffer (Expedeon)
606 and 250 mM DTT and rested for 5 min. PEG-mal accessible and non-accessible BceS were
607 analyzed by Western Blot.

608 **Western blot analysis.** Protein samples (~150 µg) from *in vivo* cross-linking and Scan-
609 SCAM were subjected to SDS-PAGE on RunBlue™ TEO-Tricine SDS mini gel in either
610 Tris-Tricine-SDS (Sigma-Aldrich) or Teo-Tricine-SDS (Expedeon) buffer, run for 50 min at
611 120V. Samples were transferred to polyvinylidene fluoride (PVDF) membranes (Merck
612 Millipore, activated in 100 % (v/v) methanol) in 1 × RunBlue SDS Running Buffer
613 (Expedeon), 20 % (v/v) methanol at 75 mA for 70 minutes using a PerfectBlue™ Sedec™
614 Semi-Dry Electroblotter (Peqlab). Membranes were blocked with 7.5 % (w/v) skimmed milk
615 powder in PBST (137 mM NaCl, 2.7 mM KCl, 10 mM Na_2HPO_4, 1.8 mM KH_2PO_4 [pH7.4],
616 0.1 % (v/v) Tween 20), washed three times in PBST, and incubated with primary antibody
617 (Penta·His Antibody, QIAGEN®, 1:2000 dilution) in 1% bovine serum albumin in PBST for
618 2h at room temperature. Following three washes in PBST, incubation with secondary
619 antibody (Peroxidase-AffiniPure Goat Anti-Rabbit IgG, Jackson ImmunoResearch Europe
620 Ltd, 1:4000 dilution) was carried out in milk-PBST for 1h at room temperature, followed by
621 three final washes in PBST. Detection of proteins was by chemiluminescence using Pierce™
622 ECL Western Blotting Substrate (Thermo Fisher Scientific Inc.) and a Qiagen CCD camera
623 with Fusion software.

624 **Homology Modelling.** Homology models for the BceS HAMP and DHp domains (positions
625 56 to 174), and for the C-terminal domain of BceAB (from position 507) were generated
626 using I-TASSER with default parameters [26]. The respective homology model with the highest
627 C-score was selected, and the top ranking structural analog from PDB identified by I-
628 TASSER was noted for reference.

629 **Gaussian-accelerated molecular dynamics (GaMD) Simulations.** A homology model of
630 the cytoplasmic region of BceS consisting of the DHp and ATPase domains was constructed
631 using I-TASSER as before [43]. The HAMP-like domain was excluded due to low sequence
632 homology with conventional HAMP domains. The approximate orientation of each BceS
633 monomer with respect to one another was predicted based on cysteine cross-linking data (Fig.
634 2) and further refined using Z-Dock to perform rigid body protein-protein docking [44], with
635 subsequent side chain rotamers optimised using SCWRL4 [45]. The N-terminus of the DHp
636 domain of each monomer was acetylated to cap the α-helix and prevent having a positive
637 charge at the termini. ATP was then docked into each ATP binding site using AutoDock Vina
638 (exhaustiveness set to 32) [46]. The generated model of BceS was then manually modified to
639 construct the E115K/K116E variant. All residues were modelled in their standard protonation
640 states, with His108 and His124 singly protonated on the Nδ1 nitrogen, and all other His
641 singly protonated on the Nε2 nitrogen (as indicated by hydrogen bonding networks). Both
642 systems were solvated in an octahedral water box such that no protein/substrate atom was
643 within 10 Å of the box boundaries, with Na^+ or Cl^- counter ions added as necessary to ensure
644 an overall neutral charge. MD simulations were performed using GPU accelerated Amber16,
645 with the ff14SB force field and TIP3P water model used to describe protein and water
646 molecules respectively. Parameters for ATP were taken from a study by Meagher and
647 colleagues [47]. Following a minimisation, heating, NVT and NPT equilibration procedure
648 (described below), Gaussian accelerated MD (GaMD) simulations were done in the NVT

649 ensemble at 300 K [28], with a boost potential applied to both the total system potential energy
650 as well as the dihedral potential energies (see also GaMD settings in Table S5). To prepare
651 for production GaMD simulations, a 12 ns long conventional MD run was used to obtain
652 maximum, minimum, average and standard deviation of the system potential energies.
653 Following this, a 66 ns long run was used to update the above parameters (updated every 600
654 ps) to ensure converged GaMD production parameters. Production GaMD simulations were
655 then run for 4 × 500 ns, using different random seeds for each replica. MD simulations were
656 run using a 2 fs time step with the SHAKE algorithm applied to any bond containing a
657 hydrogen atom. An 8 Å direct space non-bonded cut-off was applied with long-range
658 electrostatics evaluated using the particle mesh Ewald algorithm [48]. Temperature was
659 regulated using Langevin temperature control (collision frequency of 1 ps^{-1}). All MD and
660 GaMD simulations were performed with a 10 kcal mol^{-1} restraint on the Phi and Psi dihedrals
661 between the acetyl and first N-terminal residue, to prevent the α-helix fraying. Principal
662 component analysis (PCA) and other trajectory analyses were performed within CPPTRAJ [49],
663 on the Cα atoms of the DHp domain residues. PCA was performed on the trajectories after
664 constructing an average structure of all four simulations combined. Reweighting of PCA and
665 distance measurements (to obtain PMFs) was performed using the 'PyReweighting' toolkit [50].
666 To equilibrate structures for GaMD simulations, the following procedure was performed.
667 Minimisation of all hydrogen atoms and solvent molecules was done using 500 steps of
668 steepest descent followed by 500 steps of conjugate gradient. To keep all other atoms (i.e. the
669 protein heavy atoms) in place during the minimisation, 10 kcal mol^{-1} $Å^{-1}$ positional restraints
670 were applied. Retaining the positional restraints on all protein heavy atoms, the system was
671 then heated rapidly from 50 K to 300 K in the NVT ensemble over the course of 200 ps. This
672 system was again minimised for a further 500 steps of steepest descent followed by 500 steps
673 of conjugate gradient, this time only applying positional restraints (of size 5 kcal mol^{-1} $Å^{-1}$)

674 to the Cα carbon atoms. These Cα restraints were retained as the system was again heated
675 from 25 K to 300 K over the course of 50 ps in the NVT ensemble. Simulations were then
676 performed in the NPT ensemble (1 atm, 300 K), first gradually reducing the 5 kcal mol^{-1} $Å^{-1}$
677 Cα carbon restraints over the course of 50 ps of simulation time. This was done in five steps
678 (5, 4, 3, 2, 1 kcal mol^{-1} $Å^{-1}$) of 10 ps each. A final 20 ns long MD simulation was then
679 performed, in which no restraints were used, to equilibrate the box size. All dynamics steps
680 used the SHAKE algorithm. Simulations performed in the NVT ensemble used Langevin
681 temperature control (with a collision frequency of 1 ps^{-1}) and a simulation time-step of 1 fs.
682 Simulations performed in the NPT ensemble again used Langevin temperature control
683 (collision frequency of 1 ps^{-1}) and a Berendsen barostat (1 ps pressure relaxation time), with
684 a simulation time-step of 2 fs.

ACKNOWLEDGEMENTS

The authors would like to thank Roger Draheim for helpful advice in establishing the cysteine crosslinking assays. We are also grateful to our undergraduate research students Jessica Lancaster and Adam McCartan for construction of plasmids pJL705 and pAM703, respectively. We thank Jean van den Elsen and Laurence Hurst for critical reading of and feedback on the manuscript.

Work in SG's lab was supported by the Biotechnology and Biological Sciences Research Council (BBSRC; BB/M029255/1). MVdK is a BBSRC David Phillips Fellow (BB/M026280/1).

AUTHOR CONTRIBUTIONS

AK and MJG carried out all laboratory work and data analysis; MVdK and CRP performed and analyzed the MD simulations; SG supervised all laboratory work and coordinated the research project; SG, CRP and AK wrote the manuscript.

REFERENCES

1. Fritz, G. *et al.* A new way of sensing: need-based activation of antibiotic resistance by a flux-sensing mechanism. *mBio* **6,** e00975–15 (2015).
2. Dintner, S., Heermann, R., Fang, C., Jung, K. & Gebhard, S. A sensory complex consisting of an ATP-binding cassette transporter and a two-component regulatory system controls bacitracin resistance in *Bacillus subtilis*. *J Biol Chem* **289,** 27899–27910 (2014).
3. Staroń, A., Finkeisen, D. E. & Mascher, T. Peptide antibiotic sensing and detoxification modules of *Bacillus subtilis*. *Antimicrob. Agents Chemother.* **55,** 515–525 (2011).
4. Hiron, A., Falord, M., Valle, J., Débarbouillé, M. & Msadek, T. Bacitracin and nisin resistance in *Staphylococcus aureus*: a novel pathway involving the BraS/BraR two-

712 component system (SA2417/SA2418) and both the BraD/BraE and VraD/VraE ABC
713 transporters. *Mol. Microbiol.* **81,** 602–622 (2011).
714 5. Dintner, S. *et al.* Coevolution of ABC transporters and two-component regulatory
715 systems as resistance modules against antimicrobial peptides in Firmicutes bacteria. *J.*
716 *Bacteriol.* **193,** 3851–3862 (2011).
717 6. Revilla-Guarinos, A. *et al.* Characterization of a regulatory network of peptide
718 antibiotic detoxification modules in *Lactobacillus casei* BL23. *Appl. Environ.*
719 *Microbiol.* **79,** 3160–3170 (2013).
720 7. Gebhard, S. *et al.* Identification and Characterization of a Bacitracin Resistance
721 Network in *Enterococcus faecalis*. *Antimicrob. Agents Chemother.* **58,** 1425–1433
722 (2014).
723 8. Ouyang, J., Tian, X. L., Versey, J., Wishart, A. & Li, Y. H. The BceABRS Four-
724 Component System Regulates the Bacitracin-Induced Cell Envelope Stress Response
725 in *Streptococcus mutans*. *Antimicrob. Agents Chemother.* **54,** 3895–3906 (2010).
726 9. Gebhard, S. & Mascher, T. Antimicrobial peptide sensing and detoxification modules:
727 unravelling the regulatory circuitry of *Staphylococcus aureus*. *Mol. Microbiol.* **81,**
728 581–587 (2011).
729 10. Revilla-Guarinos, A., Gebhard, S., Mascher, T. & Zúñiga, M. Defence against
730 antimicrobial peptides: different strategies in Firmicutes. *Environ Microbiol* **16,** 1225–
731 1237 (2014).
732 11. Greene, N. P., Kaplan, E., Crow, A. & Koronakis, V. Antibiotic Resistance Mediated
733 by the MacB ABC Transporter Family: A Structural and Functional Perspective.
734 *Front. Microbiol.* **9,** 1923–17 (2018).
735 12. Gebhard, S. ABC transporters of antimicrobial peptides in Firmicutes bacteria -
736 phylogeny, function and regulation. *Mol. Microbiol.* **86,** 1295–1317 (2012).
737 13. Kobras, C. M. *et al.* BceAB-type antibiotic resistance transporters appear to act by
738 target protection of cell wall synthesis. *bioRxiv* **7,** 15058–36 (2019).
739 14. Gao, R. & Stock, A. M. Biological insights from structures of two-component
740 proteins. *Annu. Rev. Microbiol.* **63,** 133–154 (2009).
741 15. Gushchin, I. *et al.* Mechanism of transmembrane signaling by sensor histidine kinases.
742 *Science* **356,** eaah6345–9 (2017).
743 16. Bhate, M. P., Molnar, K. S., Goulian, M. & DeGrado, W. F. Signal Transduction in
744 Histidine Kinases: Insights from New Structures. *Structure/Folding and Design* **23,**
745 981–994 (2015).
746 17. Bhate, M. P. *et al.* Structure and Function of the Transmembrane Domain of NsaS, an
747 Antibiotic Sensing Histidine Kinase in *Staphylococcus aureus*. *J. Am. Chem. Soc.* **140,**
748 7471–7485 (2018).
749 18. Monzel, C. & Unden, G. Transmembrane signaling in the sensor kinase DcuS of
750 *Escherichia coli*: A long-range piston-type displacement of transmembrane helix 2.
751 *Proc. Natl. Acad. Sci. U.S.A.* **112,** 11042–11047 (2015).
752 19. Tetsch, L. & Jung, K. The regulatory interplay between membrane-integrated sensors
753 and transport proteins in bacteria. *Mol. Microbiol.* **73,** 982–991 (2009).
754 20. Piepenbreier, H., Fritz, G. & Gebhard, S. Transporters as information processors in
755 bacterial signalling pathways. *Mol. Microbiol.* **104,** 1–15 (2017).
756 21. Witan, J. *et al.* Interaction of the *Escherichia coli* transporter DctA with the sensor
757 kinase DcuS: presence of functional DctA/DcuS sensor units. *Mol. Microbiol.* **85,**
758 846–861 (2012).
759 22. Unden, G., Wörner, S. & Monzel, C. Cooperation of secondary transporters and sensor
760 kinases in transmembrane signalling: the DctA/DcuS and DcuB/DcuS sensor
761 complexes of *Escherichia coli*. *Adv. Microb. Physiol.* **68,** 139–167 (2016).

762 23. Hsieh, Y.-J. & Wanner, B. L. Global regulation by the seven-component P_i signaling
763 system. *Curr Opin Microbiol* **13,** 198–203 (2010).
764 24. Rietkötter, E., Hoyer, D. & Mascher, T. Bacitracin sensing in *Bacillus subtilis*. *Mol.*
765 *Microbiol.* **68,** 768–785 (2008).
766 25. Letunic, I., Doerks, T. & Bork, P. SMART 7: recent updates to the protein domain
767 annotation resource. *Nucleic Acids Res.* **40,** D302–5 (2012).
768 26. Zhang, Y. I-TASSER server for protein 3D structure prediction. *BMC Bioinformatics*
769 **9,** 76–8 (2008).
770 27. Pakula, A. A. & Simon, M. I. Determination of transmembrane protein structure by
771 disulfide cross-linking: the *Escherichia coli* Tar receptor. *Proc. Natl. Acad. Sci. U.S.A.*
772 **89,** 4144–4148 (1992).
773 28. Miao, Y., Feher, V. A. & McCammon, J. A. Gaussian Accelerated Molecular
774 Dynamics: Unconstrained Enhanced Sampling and Free Energy Calculation. *J Chem*
775 *Theory Comput* **11,** 3584–3595 (2015).
776 29. Lai, R.-Z. & Parkinson, J. S. Functional Suppression of HAMP Domain Signaling
777 Defects in the *E. coli* Serine Chemoreceptor. *J. Mol. Biol.* **426,** 3642–3655 (2014).
778 30. Hulko, M. *et al.* The HAMP Domain Structure Implies Helix Rotation in
779 Transmembrane Signaling. *Cell* **126,** 929–940 (2006).
780 31. Zhou, Q., Ames, P. & Parkinson, J. S. Biphasic control logic of HAMP domain
781 signalling in the *Escherichia coli* serine chemoreceptor. *Mol. Microbiol.* **80,** 596–611
782 (2011).
783 32. Ferris, H. U. *et al.* The Mechanisms of HAMP-Mediated Signaling in Transmembrane
784 Receptors. *Structure/Folding and Design* **19,** 378–385 (2011).
785 33. Ferris, H. U. *et al.* Mechanism of Regulation of Receptor Histidine Kinases.
786 *Structure/Folding and Design* **20,** 56–66 (2012).
787 34. Matamouros, S., Hager, K. R. & Miller, S. I. HAMP Domain Rotation and Tilting
788 Movements Associated with Signal Transduction in the PhoQ Sensor Kinase. *mBio* **6,**
789 e00616–15 (2015).
790 35. Appleman, J. A. & Stewart, V. Mutational Analysis of a Conserved Signal-
791 Transducing Element: the HAMP Linker of the *Escherichia coli* Nitrate Sensor NarX.
792 *J. Bacteriol.* **185,** 89–97 (2003).
793 36. Crow, A., Greene, N. P., Kaplan, E. & Koronakis, V. Structure and
794 mechanotransmission mechanism of the MacB ABC transporter superfamily. *Proc.*
795 *Natl. Acad. Sci. U.S.A.* **23,** 201712153–6 (2017).
796 37. Kallenberg, F., Dintner, S., Schmitz, R. & Gebhard, S. Identification of regions
797 important for resistance and signalling within the antimicrobial peptide transporter
798 BceAB of *Bacillus subtilis*. *J. Bacteriol.* **195,** 3287–3297 (2013).
799 38. Ho, S. N., Hunt, H. D., Horton, R. M., Pullen, J. K. & Pease, L. R. Site-directed
800 mutagenesis by overlap extension using the polymerase chain reaction. *Gene* **77,** 51–
801 59 (1989).
802 39. Harwood, C. R. & Cutting, S. M. *Molecular biological methods for Bacillus*. (John
803 Wiley & Sons, 1990).
804 40. Arnaud, M., Chastanet, A. & Débarbouillé, M. New vector for efficient allelic
805 replacement in naturally nontransformable, low-GC-content, Gram-positive bacteria.
806 *Appl. Environ. Microbiol.* **70,** 6887–6891 (2004).
807 41. Radeck, J. *et al.* The *Bacillus* BioBrick Box: generation and evaluation of essential
808 genetic building blocks for standardized work with *Bacillus subtilis*. *Journal of*
809 *Biological Engineering* **7,** 29 (2013).
810 42. Schindelin, J. *et al.* Fiji: an open-source platform for biological-image analysis. *Nature*
811 *Publishing Group* **9,** 676–682 (2012).

43. Yang, J. *et al.* The I-TASSER Suite: protein structure and function prediction. *Nature Publishing Group* **12,** 7–8 (2015).
44. Pierce, B. G. *et al.* ZDOCK server: interactive docking prediction of protein-protein complexes and symmetric multimers. *Bioinformatics* **30,** 1771–1773 (2014).
45. Krivov, G. G., Shapovalov, M. V. & Dunbrack, R. L. Improved prediction of protein side-chain conformations with SCWRL4. *Proteins* **77,** 778–795 (2009).
46. Trott, O. & Olson, A. J. AutoDock Vina: improving the speed and accuracy of docking with a new scoring function, efficient optimization, and multithreading. *J Comput Chem* **31,** 455–461 (2010).
47. Meagher, K. L., Redman, L. T. & Carlson, H. A. Development of polyphosphate parameters for use with the AMBER force field. *J Comput Chem* **24,** 1016–1025 (2003).
48. Darden, T., York, D. & Pedersen, L. Particle mesh Ewald: An N·log(N) method for Ewald sums in large systems. *The Journal of Chemical Physics* **98,** 10089–10092 (1993).
49. Roe, D. R. & Cheatham, T. E., III. PTRAJ and CPPTRAJ: Software for Processing and Analysis of Molecular Dynamics Trajectory Data. *J Chem Theory Comput* **9,** 3084–3095 (2013).
50. Miao, Y. *et al.* Improved Reweighting of Accelerated Molecular Dynamics Simulations for Free Energy Calculation. *J Chem Theory Comput* **10,** 2677–2689 (2014).

925 **LIST OF SUPPLEMENTAL FILES**

926 **Figure S1.** Cysteine scanning and site-directed mutagenesis of the BceS DHp domain.

927 **Figure S2.** Cysteine cross-linking following activation of signaling.

928 **Figure S3.** Equilibration and principle component analysis of Gaussian accelerated molecular
929 dynamics simulations of BceS DHp domain conformation.

930 **Figure S4.** Cysteine scanning mutagenesis of the BceS HAMP-like domain.

931 **Figure S5.** Cysteine scanning mutagenesis of the second transmembrane helix of BceS.

932 **Figure S6.** Arginine substitutions in transmembrane helix 2 of BceS.

933 **Figure S7.** Signaling phenotypes of BceAB variants.

934

935 **Table S1.** Strains used in this study

936 **Table S2.** Primers used in this study

937 **Table S3.** Plasmids used in this study

938 **Table S4.** Minimal inhibitory concentration of bacitracin in strains carrying BceAB variants

939 **Table S5.** Parameters used for GaMD simulations